Int. J. Electrochem. Sci., 15 **(2020)** 9734 – 9745, doi: 10.20964/2020.10.57

International Journal of ELECTROCHEMICAL SCIENCE
www.electrochemsci.org

Plasma-assisted Synthesis of 3-D Hierarchical Ni_2P on Ni Foam as Highly Active Hydrogen Evolution Reaction Electrocatalysts

Mojie sun[1], *Zhenye Zhang*[1], *Zhao Wang*[1], *Shiji Wang*[1], *Shiyuan Zhang*[1], *Ruiting Wang*[1], *Xiaochen Song*[2,*]

[1] School of Chemical Engineering, Northeast Electric Power University, 169# Changchun Road, Chuanying District, Jilin 132012, China
[2] School of Mechanical Engineering, Northeast Electric Power University, 169# Changchun Road, Chuanying District, Jilin 132012, China
[*]E-mail: songxiaochen0306@163.com

Received: 5 July 2019 / *Accepted:* 11 August 2020 / *Published:* 31 August 2020

To prepare low-cost, high-performance electrocatalytic hydrogen evolution material, we prepared Ni_2P nanosheets on nickel foam (NF) substrate combining the hydrothermal method and plasma-enhanced chemical vapor deposition (PECVD). We characterized the microstructure and composition of the material with X-ray diffraction (XRD), Field Emission Scanning Electron Microscopy (SEM), and Energy Dispersive Spectroscopy (EDS). Meanwhile, the electrochemical properties of the material under acidic and alkaline conditions were tested. In 0.5 M H_2SO_4 solution, the current density was 10 mA/cm^2, and the potential was 106 mV; in 1 M KOH solution, the current density was 10 mA/cm^2, and the potential was 97 mV. The results demonstrate that the nanoflake Ni_2P/NF as-prepared has good electrocatalytic activity under either acidic or alkaline conditions.

Keywords: Ni_2P; electrocatalysis; plasma synthesis; HER

1. INTRODUCTION

Energy is the main driving force for the rapid development of society and the economy today. However, due to the excessive use of energy, the problem of environmental pollution has become increasingly severe [1-2]. At present, the energy sources that are widely used in practice are mainly traditional energy sources that are harmful to the environment, such as coal, natural gas, and petroleum [3-5]. These energy sources all cause serious pollution to the environment, making it impossible for them to continue to be used in future energy systems. The current social energy crisis and environmental problems are already very serious. Therefore, it is imperative to study and develop green and efficient clean energy [6-8]. Hydrogen (H_2) energy, a clean and renewable secondary energy, meets the needs of energy development and the environment and is an ideal substitute for fossil fuels.

Therefore, it will play a very important role in the future energy pattern [9-10].

Nickel phosphide (Ni_2P) is a highly efficient HDS catalyst [11]. Ni2P can generate H_2 by water vapor displacement reaction [12], and Ni_2P conforms to hexagonal Fe_2P structure. In addition, it can be known from the density functional theory calculation that the Ni and P sites exposed on the surface of $Ni_2P(001)$ exhibit a holistic effect, in which both the proton acceptor and the hydride acceptor center exist to promote the catalysis of HER.

Electrolysis of water to hydrogen is an ideally suited method to produce hydrogen due to its high efficiency, no pollution and abundant raw materials [13]. Efficient and stable catalysts facilitate the electrolysis of water and greatly accelerate the two and a half reactions of electrocatalytic hydrogen evolution and electrocatalytic oxygen evolution (HER and OER). Although traditional noble metal electrodes have a low hydrogen evolution potential, their cost is too high and sources are scarce, which limits the development of hydrogen production from electrolyzed water [14-16]. Transition metal compound electrodes have good electrocatalytic hydrogen evolution properties, such as MoS_2 [17], NiS [18], cobalt CoP [19], Ni_2P [20-23], etc. However, they have lower catalytic performance than noble metal electrodes. It has been shown that the effective ways to improve the electrocatalytic performance are to increase the specific surface area, conductivity and number of active sites exposed to the catalyst. Paseka [24] made Ni-P alloy by electrodeposition. Studies have shown that, when the mass fraction of P is 3%, the electrocatalytic activity of the hydrogen evolution of the alloy electrode is the highest, but the increase in P content will lead to the decline of its activity. Raymond E. Schaak [25] prepared nanoscale Ni_2P materials using the oil phase method. It was found that Ni_2P nanoparticles can act as a highly efficient electrochemical hydrogen evolution catalyst in acidic media, and the Faradaic efficiency of hydrogen production approaches 100%. Stephanie L. Brock's group [26] synthesized three-dimensional Ni_2P nanoparticles, where the sol-gel oxidation method is first used to form P-O-P bonds between phosphorus particles and the surface of the mesh particles. Metal-mediated condensing is then used to bind the metal ion to the surface of the carboxylate functional group to bind it with the thiolate ligand, resulting in reticulated nanostructured particles.

In this study, nickel-phosphorus electrocatalytic materials were in situ grown on the substrate surface via the hydrothermal method and PECVD method [27-28].

This type of material has the electrical conductivity of metal and has the advantages of high mechanical strength and high stability. Additionally, because foamed nickel has a porous character, it can effectively increase the specific surface area of the material. The use of PECVD enables the surface of the catalyst to be exposed to more active sites and can yield better electrocatalytic performance in the same environment.

2. EXPERIMENTS

2.1 Synthesis of Ni_2P/NF

In this experiment, a new type of Ar plasma-enhanced chemical vapor deposition was used to synthesize a nickel hydroxide ($Ni(OH)_2$) precursor prepared by the hydrothermal method into a Ni_2P nanostructure. The synthesis of Ni_2P/NF porous nanoplates was as follows. Ni hydroxide ($Ni(OH)_2$)

precursor was hydrothermally synthesized on Ni foam (typically 2 × 3 cm), which was precleaned by concentrated HCl, washed by acetone, ethanol, and demineralized water, and then removed and vacuum dried for 6 hours. In a typical synthesis, 1.7 g of NH_4NO_3 were dissolved in 50 mL of distilled water. The solution was stirred for 10 min before transferring to a 50-mL autoclave, Then, the autoclave was sealed and heated in a blast drying oven at 90°C for 24 hours. The Ni hydroxide was then thermally phosphorized to yield Ni_2P porous nanoplates through a novel Ar gas plasma-assisted approach. Briefly, the Ni foam covered with precursor material and sodium hypophosphite was placed in the reaction chamber of a plasma-enhanced chemical vapor deposition (PECVD) system, followed by Ar plasma treatment at 250℃ for 60 min, and then naturally cooled to ambient temperature. The conditions for the plasma were Ar flux of 50 sccm and power of 60 W.

2.2 Physical Characterization

Powder X-ray diffraction (XRD) data were recorded on an XRD-700 diffractometer. Measurements were performed on a Helios NanoLab 600i microscope using a scanning electron microscope (SEM), and X-ray photoelectron spectroscopy (XPS, Perkin-Elmer PHI5300X) was used to characterize the valence of different elements in a material.

2.3 Electrochemical measurements

The electrochemical test was carried out at 25°C using a three-electrode system. The prepared Ni_2P/NF (1 cm^2) was used as the working electrode, the graphite sheet was the counter electrode, and the saturated calomel electrode (SCE) was used under acidic (0.5 M H_2SO_4) conditions. The mercury oxide electrode (Hg/HgO) is a reference electrode under alkaline conditions (1 M KOH). Cyclic voltammetry (CV), linear voltammetric scanning (LSV), chronopotential (e-t) and alternating current impedance (EIS) tests were performed on Ni_2P/NF. The data $E_{(SCE)}$ or $E_{(Hg/HgO)}$ obtained by the test are all converted to the potential $E_{(RHE)}$ at the reversible hydrogen electrode. In 0.5 M H_2SO_4, $E_{RHE}=E_{SCE}+E^0_{SCE}+0.0591$ pH. In 1 M KOH, $E_{RHE}=E_{Hg/HgO}+E^0_{Hg/HgO}+0.0591$ pH. The Tafel slope is linearly fitted to the straight line in the Tafel diagonal line, which satisfies the Tafel formula: $\eta=a\log(j)+b$.

3. RESULTS AND DISCUSSION

Figure 1-A and 1-B show the XRD patterns of $Ni(OH)_2$/NF (Solvent heat) and Ni_2P/NF-PECVD. The strong diffraction peaks at 44, 52, and 76 arise from the NF substrate (JCPDS#87-0712). Figure 1a shows the characteristic peaks at 19.2, 33.1, 38.5, 39.1, 52.1, 59.1, 60.7, 62.7, 70.4, 72.7, and 73.1. These characteristic peaks correspond to six square phase $Ni(OH)_2$ (JCPDS#14-0117). As seen from Figure 1b, after PECVD treatment of $Ni(OH)_2$, eight characteristic peaks appear in the XRD pattern. Their locations are in 40.8, 44.6, 47.3, 54.2, 54.9, 66.2, 72.7, and 74.7. These eight characteristic peaks correspond to six square phase Ni_2P (111), (201), (210), (300), (211), (310), (311) and (400) crystal faces, respectively, a match with the Ni_2P standard card (JCPDS#03-0953). It is

indicated that the PECVD reaction can successfully convert the precursor $Ni(OH)_2$ to Ni_2P under low-temperature conditions.

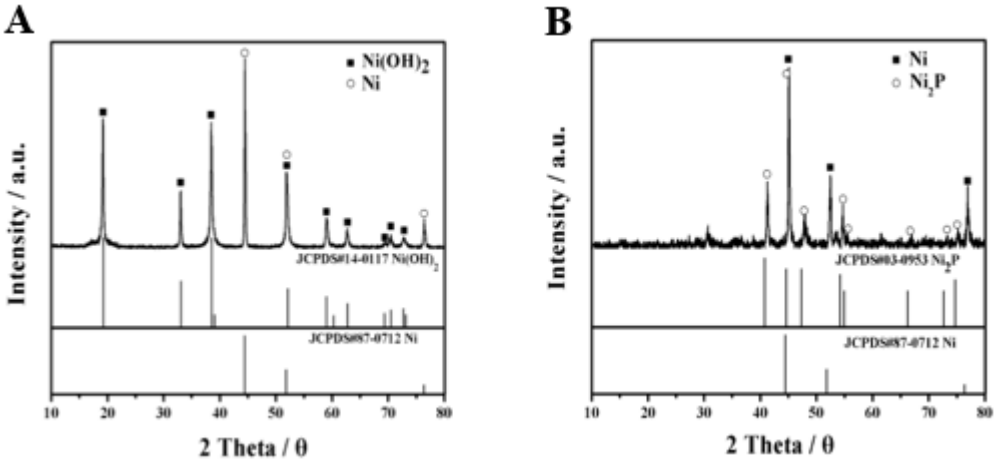

Figure 1. (A) XRD patterns of $Ni(OH)_2$/NF. (B) XRD patterns of Ni_2P/NF.

As illustrated in Figure 2-A, the synthesized $Ni(OH)_2$ is in-situ grown on the surface of nickel foam with a thickness of 3 μm. The SEM images of $Ni(OH)_2$/NF (Figure 2-B) show that the entire surface of the NF was covered with $Ni(OH)_2$/NF. The subsequent phosphatization leads to Ni_2P/NF film-coated NF (Figure 2-C). In Figure 2-B, it can be seen that its growth part is a lamellar structure with a thickness of 50 nm. The specific surface area of the material is increased to help improve the electrocatalytic performance. From Figure 2-C, it can be seen that the micromorphology of Ni_2P/NF prepared by plasma-enhanced chemical deposition at 250℃ can maintain the lamellar structure, which is in situ on the NF surface, with a thickness of approximately 100 nm. The lamellar structure contributes to the exposure of active sites, enlarges the specific surface area of the material, and improves the electrocatalytic hydrogen evolution of the electrode. As seen from Figure 2-D, the sample was subjected to an EDS test showing the atomic ratio of the surface of the material. The observed oxygen element comes from the surface of the nickel foam.

The synthesized Ni_2P/NF was characterized by X-ray photoelectron spectroscopy (XPS). The chemical states of Ni, P, and C in Ni_2P/NF were investigated as shown in Fig. 3. The XPS measurement spectrum (Fig. 3-A) confirmed the elemental composition of Ni_2P/NF, in which the peaks of P, Ni, O, and C were present. It can be seen from Fig. 3-B that four satellite peaks appear at 284.7, 285.5, 286.8 and 289.1 eV, which can be assigned to an sp2 hybrid carbon atom, and the graphite-like sp3 hybrid carbon atom and the carbon atom are bound to one. Single and double bonds of oxygen atoms [29]. In Figure 3c, it can be seen that six peaks can be observed at 854.0, 856.9, 858.0, 861.2, 874.9 and 880.2 eV, Among them, the four peaks at 854.0, 856.9, 858.0 and 861.2 eV represent the Ni $2p_{3/2}$ energy level, which can be attributed to Ni in Ni_2P, oxidized Ni species and the satellite of the Ni $2p_{3/2}$ peak [30]. The Ni $2p_{1/2}$ level has two peaks at 874.9 eV and 880.2 eV (Fig. 3-C), corresponding to Ni on Ni_2P, oxidized Ni and Ni $2p_{1/2}$ peak satellites, respectively. For P and 2p energy levels, as shown in Figure 3, two satellite peaks appear at 134.0 and 135.0 eV, due to P in Ni_2P and oxidized P on the surface of the Ni_2P/NF nanomixture due to air contact [31]. Ni_2P/NF has similar

C 1s, Ni 2p and P 2p levels to $Ni_{12}P_5$/NF [32]. The Ni $2p_{3/2}$ satellite peak appearing at 854.0 eV is very close to the satellite peak of metal Ni, indicating that the Ni species in Ni_2P has a very small positive charge ($Ni^{\delta+}$, $0<\delta<2$). The binding energy of P 2p at 135.0 eV is smaller than that of elemental P (135.0 eV), indicating that P species in Ni_2P have a small negative charge ($P^{\delta-}$, $0<\delta<1$). Therefore, from Figure 3-D, we can conclude that there is electron transfer from Ni to P and that small charges represent major covalent features with small ion contributions.

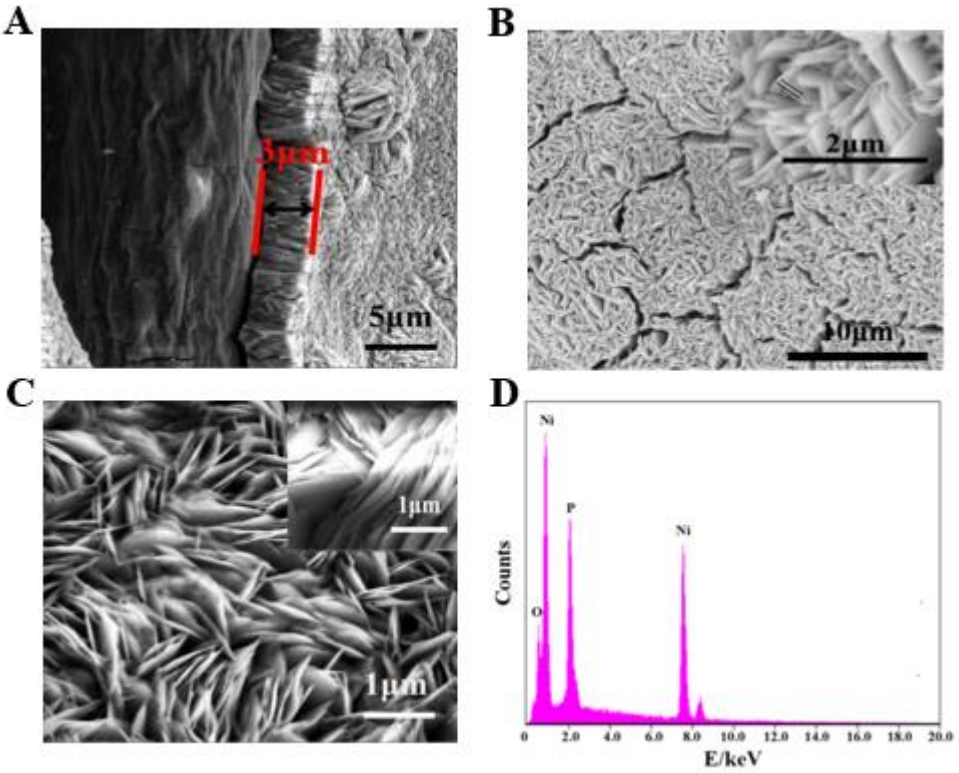

Figure 2. (A) The SEM images of $Ni(OH)_2$/NF side. (B) Low- and high (inset)-magnification SEM images of $Ni(OH)_2$/NF. (C) Low- and high (inset)-magnification SEM images of Ni_2P/NF. (D) EDS spectrum of Ni_2P/NF.

We evaluated the HER catalytic activity of Ni_2P/NF as a hydrogen evolution cathode in 0.5 M H_2SO_4 or 1 M KOH with a scan rate of 5 mV s^{-1}. Figure 4-A is the LSV curve obtained from a Ni_2P/NF electrode in 0.5 M H_2SO_4 solution. For the comparison study, blank NF and Ni_2P/NF by the traditional gas phase deposition method were also examined. Figure 4a shows the polarization curves. It can be seen from the graph that the current density of the Ni_2P/NF obtained by the PECVD method reaches 10 mA/cm^2 at 106 mV, while the Ni_2P/NF prepared by the traditional gas phase deposition method needs to be reached when the overpotential reaches 168 mV. Figure 4-B shows that the Tafel slope of Ni_2P/NF-PECVD is 79 mV/dec, and the electrocatalytic rate of Ni_2P/NF is faster than that of Ni_2P/NF prepared by ordinary vapor deposition. Figure 4-C is the LSV curve comparison of Ni_2P/NF-PECVD after a rapid (0.5 V/s) and multicycle (500 cycles) scan by cyclic voltammetry. After analysis, the electrocatalytic activity of the material has been improved after 500 cycles of cyclic voltammetry. Figure 4-D is the stability test of the material with a current density of 10 mA/cm^2. The analysis of the

E-T curve shows that the overpotential of Ni_2P/NF-PECVD has a small change in the 12-h test and good stability. Figure 4-E is the AC impedance of different materials. Through the impedance diagram, it can be seen that the impedance map of the Ni_2P/NF produced by the PECVD method has a smaller radius, so it has a smaller resistance. It can be seen from the SEM image that the material prepared by PECVD has a large specific surface area, which facilitates electrolyte penetration and provides more exposed active sites [33]. To prove this inference, the electric double-layer capacitance (C_{dl}) was tested by simple cyclic voltammetry (CV) at different scanning speeds to evaluate the electrochemical active area (ECSA) of different electrocatalysts. The interval in which the redox process occurs can better evaluate ECSA [34]. Figure 4-F and G are cyclic voltammograms of Ni_2P/NF and Ni_2P/NF-PEVCD at different scan rates (5-150 mV/s), respectively. Select the maximum current and minimum current at the intermediate potential and calculate them. The difference between the two is obtained in Figure 4-H. As shown in Figure 4-H, the difference in the current density of the different catalysts is linear with the scan rate. The C_{dl} size of Ni_2P/NF is 7.426 mF, and the C_{dl} size of Ni_2P/NF-PEVCD is 28.743 mF. Therefore, it proves that our inference is correct, which is one of the reasons why the catalyst has high activity.

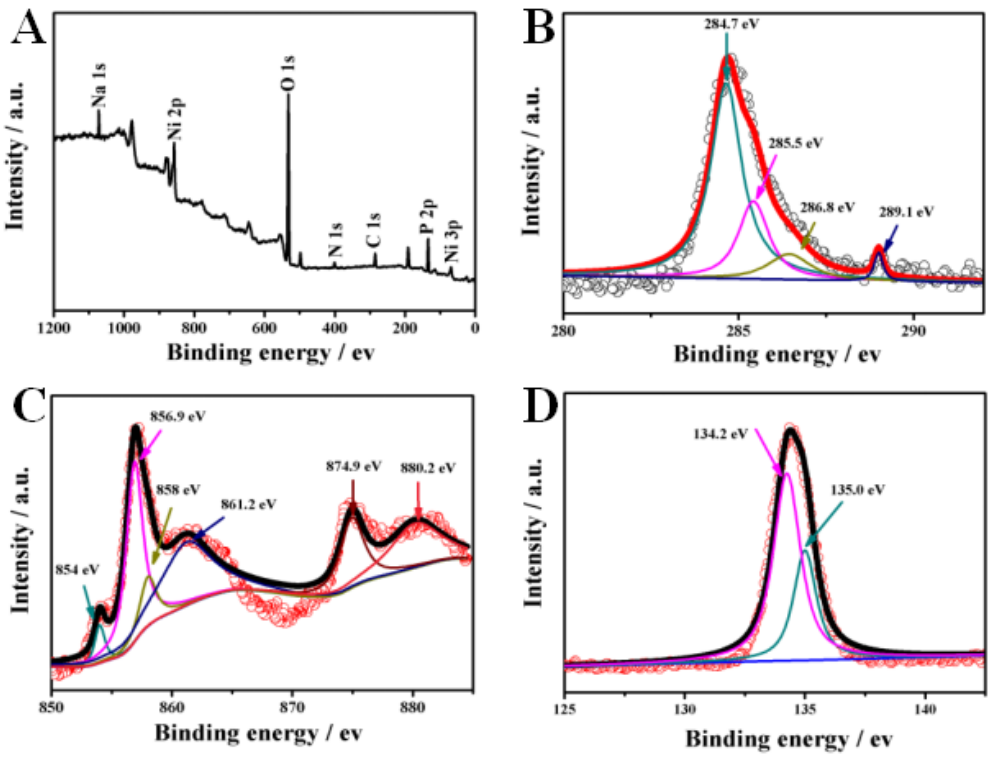

Figure 3. XPS characterization of the Ni_2P. (A) survey spectrum, (B) C 1s spectra, (C) Ni 2p spectra and (D) P 2p spectra of the Ni_2P.

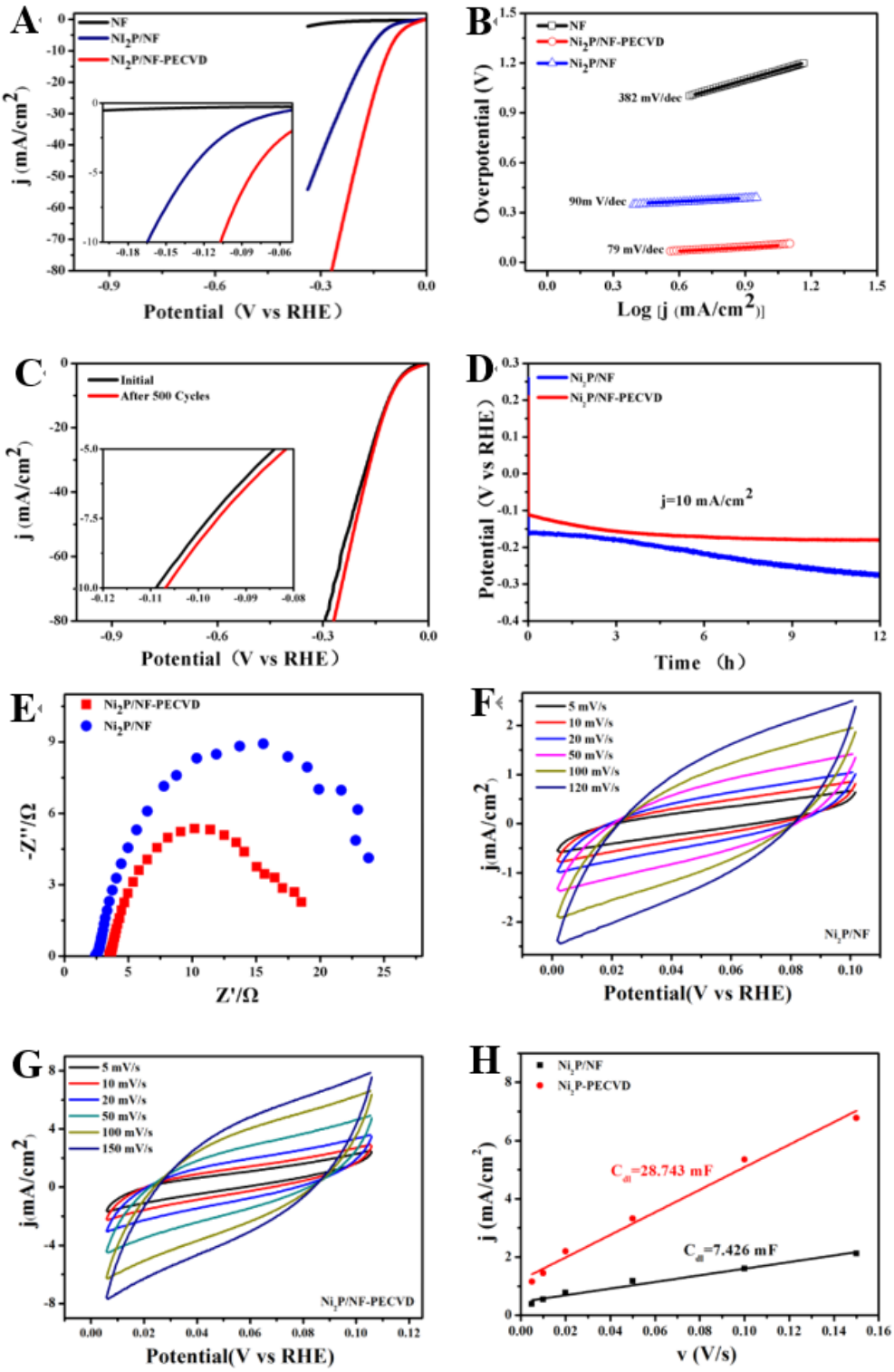

Figure 4. Hydrogen evolution reaction electrocatalysis in 0.5 M H_2SO_4. (A) IR-corrected polarization curves per geometric area of the Ni_2P/NF-PECVD recorded at a scan rate of 5 mV/s, along with Ni_2P/NF, Ni_2P/NF-PECVD, and NF for comparison. (B) Polarization curve-derived Tafel slopes for the corresponding electrocatalysts. (C) The change of hydrogen evolution potential after 500 cycles of activation (D) Long-term stability test carried out under a constant current density of -10 mA/cm^2. (E) Comparison of current impedance. (F) Ni_2P/NF-CVD CV chart at different scan rates. (G) Ni_2P/NF-PECVD chart at different scan rates. (H) Electrochemical active area comparison chart.

Figure 5 shows the electrocatalytic performance of Ni_2P/NF-PECVD under alkaline (1 M KOH) conditions. Figure 5-A and 5-B are the LSV curves and Tafel curves of Ni_2P/NF prepared by Ni_2P/NF-PECVD and ordinary vapor deposition. By contrast, the overpotential of Ni_2P/NF-PECVD at a current density of 10 mA/cm^2 is 97 mV, which is approximately 70 mV lower than the overpotential of ordinary Ni_2P/NF, and has a relatively low Tafel slope. Analysis of Figure 5-C shows that the electrocatalytic performance of Ni_2P/NF-PECVD can also be improved after 500 cycles of activation scanning in alkaline conditions. Figure 5-D was used to test the electrocatalytic stability. It was found that there was no significant change in the hydrogen evolution overpotential after 12 h in alkaline conditions, and the electrode was stable. It can be seen from the impedance diagram of Figure 5-E that Ni_2P/NF has larger resistance in alkaline conditions, but the material prepared by the PECVD method is relatively small. Figure 5-F and G are cyclic voltammograms of Ni_2P/NF and Ni_2P/NF-PEVCD at different scan rates (5-150 mV/s), respectively. Select the maximum current and minimum current at the intermediate potential and calculate their difference; the result is shown in Figure 5-H. As shown in Figure 5-H, the difference in current density between the different catalysts is linear with the scan rate. The C_{dl} size of Ni_2P/NF is 6.233 mF, and the C_{dl} size of Ni_2P/NF-PEVCD is 24.163 mF. Therefore, it was confirmed that the material prepared by PECVD also has a large electrochemical specific surface area in an alkaline solution [35].

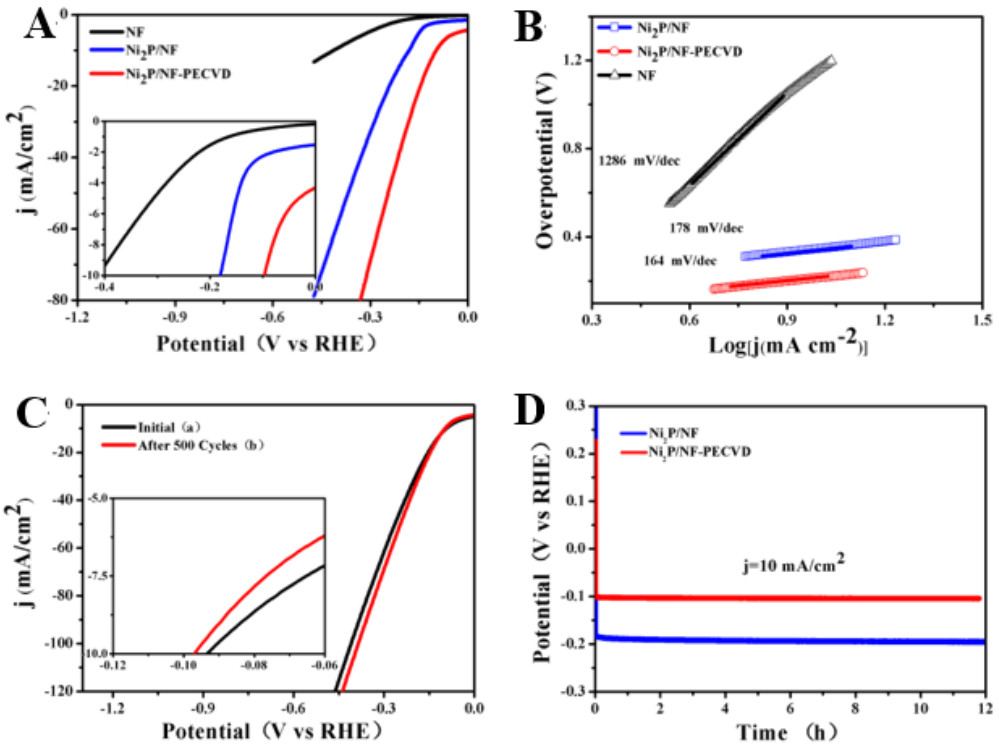

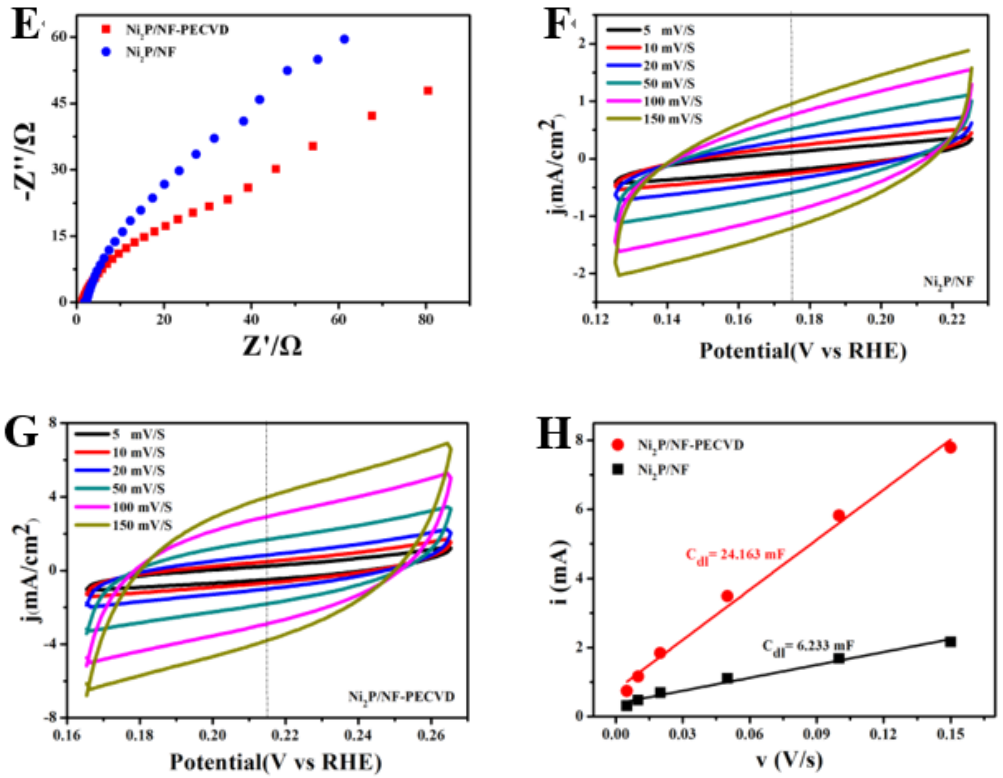

Figure 5. Hydrogen evolution reaction electrocatalysis in 1 M KOH. (A) IR-corrected polarization curves per geometric area of the Ni_2P/NF-PECVD recorded at a scan rate of 5 mV/s, along with Ni_2P/NF, Ni_2P/NF-PECVD, and NF for comparison. (B) Polarization curve-derived Tafel slopes for the corresponding electrocatalysts. (C) The change of hydrogen evolution potential after 500 cycles of activation (D) Long-term stability test carried out under a constant current density of -10 mA/cm^2. (E) Comparison of current impedance. (F) Ni_2P/NF-CVD CV chart at different scan rates. (G) Ni_2P/NF-PECVD chart at different scan rates. (H) Electrochemical active area comparison chart.

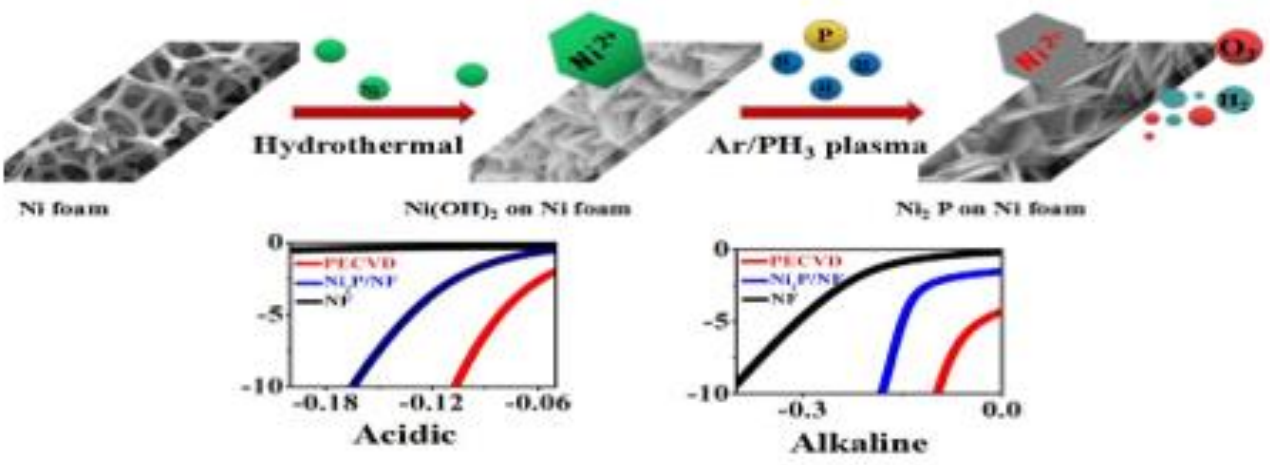

Figure 6. Schematic diagram of the material synthesis process and hydrogen evolution potential in different electrolytes.

Table 1. Summary of representative HER catalysts

Catalyst	η (mV) at J = 10 mA cm^{-2}	Electrolyte Solution	Reference
Ni_2P/NF	97	1 M KOH	This Work
Ni_2P/NF	106	0.5 M H_2SO_4	This Work
Ni_2P/NF	~150	1 M KOH	36
Ni_2P/Ni/NF	98	1 M KOH	37
CoP_3/Ni_2P	115	0.5 M H_2SO_4	38
Ni_2P	168	1 M KOH	39
NiS/Ni_2P/CC	111	1 M KOH	40
Ni_2P/CC	126	1 M KOH	40
MOF-Ni_2P	158	0.5 M H_2SO_4	41
Ni_2P	240	0.5 M H_2SO_4	42

4. CONCLUSIONS

In summary, the tests of LSV, E-T, and EIS on Ni_2P/NF-PECVD showed that the Ni_2P/NF prepared by this study had good electrocatalytic activity and stability in a larger pH range. This is attributed to the activation of the plasma to the gas that can make the reaction take less time under the lower temperature. The reaction can maintain the microstructure of the material better and make the material have a larger specific surface area. The irregular motion after the gas is activated can effectively make the defect on the surface of the material and make the active position of the material. The point is more exposed. The synthesis of the transition metal compounds provides a new direction for exploring catalysts with higher electrocatalytic activity.

ACKNOWLEDGMENTS
This work was supported by the National Natural Science Foundation of China (Grant No., 61603086), Science and Technology Development Fund of Jilin Province, China (20170204015SF), and Jilin City Science and Technology Innovation Development Plan (201750212).

References

1. A. L. Goff, V. Artero, B. Jousselme, P. D. Tran, N. Guillet, R. Metaye, A. Fihri, S. Palacin, M. Fontecave, *Science,* 326 (2009) 1384.
2. J. X. Feng, J. Q. Wu, Y. X. Tong, G. R. Li, *J. Am. Chem.,* 140 (2018) 610.

3. J. Yu, F. X. Ma, Y. du, P. P. Wang, C. Y. Xu, L. Zhen, *ChemElectroChem,* 4 (2017) 594.
4. K. Y. Zhang, W. H. Liu, H. Chen, B. Zhang, J. G. Liu, C. W. Liu, *Chem. Ind. Eng. Pro.,* 34 (2015) 3680.
5. L. B. Zhang, J. R. Cheng, D. C. Huang, L. Zhao, *Mod. Phys.,* 16 (2004) 11.
6. A. Kargar, K. Sun, Y. Jing, C. Choi, H. Jeong, G. Y. Jung, S. Jin, D. Wang, *Acs Nano,* 7 (2013) 9407.
7. Z. Xing, D. Wang, Q. Li, A. M. Asiri, X. Sun, *Electrochim. Acta,* 210 (2016) 729.
8. P. Moni, S. Hyun, A. Vignesh, S. Shanmugam, *Chem. Commun.,* 53 (2017) 7836.
9. M. H. Hansen, L. A. Stern, L. Feng, J. Rossmeisl, X. Hu, *Phys. Chem. Chem. Phys.,* 17 (2015) 10823.
10. M. G. Walter, E. L. Warren, J. R. McKone, S. W. Boettcher, Q. Mi, E. A. Santori, N. S. Lewis, *Chem. Rev.,* 110 (2010) 6446.
11. P. Liu, J. A. Rodriguez, T. Asakura, J. Gomes, K. Nakamura, *J. Phys. Chem. B,* 109 (2005) 4575.
12. P. Liu, J. A. Rodriguez, Y. Takahashi, K. Nakamura, *J. Catal.,* 262 (2009) 294.
13. L. Jiao, Y. X. Zhou, H. L. Jiang, *Chem. Sci.,* 7 (2016) 1690.
14. Y. Pan, Y. Liu, J. Zhao, K. Yang, J. Liang, D. Liu, W. Hu, D. Liu, Y. Liu, C. Liu, *J. Mater. Chem. A,* 3 (2015) 1656.
15. Q. He, X. Chen, S. Chen, L. Liu, F. Zhou, X. B. Li, G. Wang, *ACS Appl. Mater. Interfaces,* 11 (2019) 2944
16. Z. Xing, Q. Li, D. Wang, X. Yang, X. Sun, *Electrochim. Acta,* 191 (2016) 841.
17. M. Chhetri, U. Gupta, L. Yadgarov, R. Rosentsveig, R. Tenne, C. N. R. Rao, *Dalton Trans.,* 44 (2015) 16399.
18. T. An, Y. Wang, J. Tang, W. Wei, X. Cui, A. M. Alenizi, L. Zhang, G. Zheng, *J. Mater. Chem. A,* 4 (2016) 13439.
19. H. Yang, Y. Zhang, F. Hu, Q. Wang, *Nano Lett.,* 15 (2015) 7616.
20. J. Zheng, W. Zhou, T. Liu, S. Liu, C. Wang, L. Guo, *Nanoscale,* 9 (2017) 4409.
21. C. Du, M. Shang, J. Mao, W. Song, *J. Mater. Chem. A,* 5 (2017) 15940.
22. Y. Shi, Y. Xu, S. Zhuo, J. Zhang, B. Zhang, *ACS Appl. Mater. Interfaces,* 7 (2015) 2376.
23. Y. Zhang, Y. Liu, M. Ma, X. Ren, Z Liu, G Du, A. M. Asiri, X. Sun, *Chem. Commun.,* 53 (2017) 11048.
24. I. Paseka, *Electrochim. Acta,* 40 (1995) 1633.
25. E. J. Popczun, J. R. McKone, C. G. Read, A. J. Biacchi, A. M. Wiltrout, N. S. Lewis, R. E. Schaak, *J. Am. Chem. Soc.,* 135 (2013) 9267.
26. A. H. Mudiyanselage, K. Senevirathne, S. L. Brock, *Chem. Mat.,* 26 (2014) 6251.
27. A. Wang, M. Qin, J. Guan, L. Wang, H. Guo, X. Li, Y. Wang, R. Prins, Y. Hu, *Angew. Chem.,* 120 (2008) 6141.
28. H. Liang, A. N. Gandi, D. H. Anjum, X. Wang, U. Schwingenschlogl, H. N. Alshareef, *Nano Lett.,* 16 (2016) 7718.
29. W. Qiu, J. Xia, S. He, H. Xu, H. Zhong, L. Chen, *Electrochim. Acta,* 117 (2014) 145.
30. A. P. Grosvenor, S. D. Wik, R. G. Cavell, A. Mar, *Cheminform,* 37 (2006) 8988
31. J. Wang, Q. Yang, Z. Zhang, S. Sun, *Chem.-Eur. J.,* 16 (2010) 7916.
32. Y. Pan, Y. Liu, J. Zhao, K. Yang, J. Liang, D. Liu, W. Hu, D. Liu, Y. Liu, C. Liu, *J. Mater. Chem. A,* 3 (2015) 1656.
33. L. Youseff, S. Roualdes, J. Bassil, M. Zakhour, V. Rouessac, C. Lamy, M. Nakhl, J. Appl. Electrochem., 49 (2019) 135.
34. Y. Lu, J. Tu, C. Gu, X. Wang, S. X. Mao, J. Mater. Chem., 21 (2011) 17988.
35. L. Wang, C. Gu, X. Ge, J. Zhang, H. Zhu, J. Tu, ChemNanoMat, 4 (2017) 124.
36. P. E. R. Blanchard, A. P. Grosvenor, R. G. Cavell, A. Mar, *Chem. Mat.,* 20 (2008) 7081.
37. B. You, N. Jiang, M. Sheng, W. Bhushan, Y. Sun, *ACS Catal.,* 6 (2015) 714
38. K. Wang, X. She, S. Chen, H. Liu, D. Li, Y. Wang, H. Zhang, D. Yang, X. Yao, *J. Mater. Chem. A,*

6 (2018) 5560.
39. Q. Wang, Z. Liu, H. Zhao, H. Huang, H. Jiao, Y. Du, *J. Mater. Chem. A,* (2018).
40. X. Xiao, D. Huang, Y. Q. Fu, M. Wen, X. Jiang, X. Lv, M. Li, L. Gao, S. Liu, M. Wang, C. Zhao, Y. Shen, *ACS Appl. Mater. Interfaces,* 10 (2018) 4689.
41. L. Yan, P. Dai, Y. Wang, X. Gu, L. Li, L. Cao, X. Zhao, *ACS Appl. Mater. Interfaces,* 9 (2017) 11642.
42. G. Wang, H. Zheng, X. Huang, Z. Wu, H. Gao, W. Dong, *Chem.-Asian J.,* 12 (2017) 2956.